Macroscopic effect of plasmon-driven high-order-harmonic generation

Feng Wang,[1] Weiwei Liu,[1] Lixin He,[1] Liang Li,[1] Baoning Wang,[1] Xiaosong Zhu,[1] Pengfei Lan,[1,*] and Peixiang Lu[1,2,†]

[1]*School of Physics and Wuhan National Laboratory for Optoelectronics, Huazhong University of Science and Technology, Wuhan 430074, China*

[2]*Laboratory of Optical Information Technology, Wuhan Institute of Technology, Wuhan 430205, China*

(Received 5 June 2017; published 12 September 2017)

We present a numerical method to calculate the macroscopic harmonic spectrum generated from the gas-exposed nanostructure. This method includes the propagation of plasmonic and harmonic fields in the macroscopic medium as well as the response of the single atom exposed to plasmonic field. Based on the simulation, we demonstrate that the macroscopic harmonic yields drop dramatically in the high-energy region. This result well interprets the disagreement in the cutoff between the single-atom prediction and the experimental detection. Moreover, we also show that the harmonic cutoff difference induced by a π shift in carrier-envelope phase (CEP) of laser pulses depends sensitively on the spatial position. However, when the collective effect of plasmon-driven high-order-harmonic generation is considered, this cutoff difference is eliminated.

DOI: 10.1103/PhysRevA.96.033407

I. INTRODUCTION

High-order-harmonic generation (HHG) through the interaction of intense laser pulses with atomic or molecular gases is regarded as an effective way to produce the coherent extreme ultraviolet, soft x-ray, and attosecond pulses [1–4]. The few-cycle pulses generated by the OPA process [5] is one of the tools to produce the isolated attosecond pulse [6]. These ultrashort pulses play a key role in probing ultrafast electronic dynamics inside atoms [7,8], molecules [9–14], and solids [15–17].

HHG is a highly nonlinear conversion process; the minimal laser intensity for HHG is on the order of 10 TW/cm^2. To exceed this threshold, the chirped pulse amplification (CPA) system is usually adopted to raise the peak power of femtosecond pulses emitting from an oscillator. However, the CPA system limits the repetition rate of laser pulses to the low kilohertz region. Recently, the plasmon-driven HHG in the vicinity of the metallic nanostructure has attracted wide attention. This way could enhance the intensity of the incident laser pulse by more than two orders, which allows one to attain laser intensities needed for HHG directly from a moderate-power femtosecond oscillator [18–21]. It not only removes the bulky CPA system, but also gives a way to generate attosecond pulses at high repetition rates [22,23]. By using an array of bow-tie nanostructures, Kim *et al.* [18] first experimentally demonstrated that the high harmonics with wavelengths from the 7th (114 nm) to 17th (47 nm) can be generated. However, due to the inefficient harmonic emissions, the plasma atomic lines can overpower the harmonic signals [24]. Therefore, the outcome of Kim's experiment has been subject to an intense controversy since it was reported [25,26]. Fortunately, alternative approaches to realize efficient plasmon-driven HHG have been explored by employing different kinds of nanostructures [22] or using a solid tip as the HHG emitter instead of gas atoms [20]. Due to the promising applications of plasmon-driven HHG, a number of researches have been carried out [27–30].

For plasmon-driven HHG, the laser fields in the interaction region where the high harmonics are generated are spatially inhomogeneous. By using the linearly spatial-dependent laser fields, researchers have discovered some novel characteristics of the plasmon-driven HHG, for instance, the selection of quantum paths [31–33], the extension of the cutoff [34–36], and the cutoff difference induced by a π shift in CEP of laser pulses [37,38], etc. It's worth noting that due to the narrow interaction region in the nanogap, most previous studies on plasmon-driven HHG mainly focus on the response of the single atom exposed to the laser field, while the HHG process includes both the single-atom response and also the copropagation of the laser and harmonic fields in the macroscopic medium. Even though the single-atom harmonic spectrum has revealed some attractive phenomena of plasmon-driven HHG, it is still obviously different from the experiment [18]. For a better comparison with the experiment, Yavuz [39] has investigated the single-atom harmonic spectra at the different spatial points and presented that for a given population distribution, the harmonic cutoff at a certain spatial point is in qualitative agreement with the experiment. Yet, the harmonic emission in the vicinity of the nanostructure is the coherent superposition of contributions from different spatial points. It's still crude to describe the collective effect with the harmonic emission only at one point. However, a comprehensive description including the single-atom and macroscopic responses of HHG from the nanostructure has scarcely been reported.

In this paper, we present a numerical method to calculate the plasmon-driven macroscopic harmonic spectrum. Our method is based on solving the three-dimensional Maxwell equations for the propagation of plasmonic and harmonic fields as well as the time-dependent Schrödinger equation for the single-atom response of HHG. The results show that the macroscopic harmonic yields drop dramatically in the high-energy region. It well clarifies the disagreement in the cutoff between the single-atom prediction and the experimental detection [18]. On the other hand, we also find that the cutoff difference induced by a π shift in the CEP of the laser pulse depends sensitively on the spatial position and this cutoff difference is eliminated

*pengfeilan@mail.hust.edu.cn
†lupeixiang@mail.hust.edu.cn

by considering the macroscopic response of plasmon-driven HHG.

II. THEORETICAL MODEL

A. Finite-difference time-domain simulation of plasmonic fields

In our calculation, we first solve the three-dimensional Maxwell equations for the propagation of plasmonic field in the nanostructure. The Maxwell curl equations are given by

$$\nabla \times \vec{H}(x,y,z,t) = \frac{\partial \vec{D}(x,y,z,t)}{\partial t} + \vec{J}(x,y,z,t), \quad (1)$$

$$\nabla \times \vec{E}(x,y,z,t) = -\frac{\partial \vec{B}(x,y,z,t)}{\partial t} - \vec{J}_m(x,y,z,t), \quad (2)$$

where $\vec{E}$ and $\vec{H}$ are the electric and magnetic vectors, $\vec{D}$ and $\vec{B}$ are the electric displacement and magnetic inductive. $\vec{J}$ and $\vec{J}_m$ are electric and magnetic current densities. The constitutive relations in the linear and isotropic materials are $\vec{D} = \varepsilon \vec{E}$, $\vec{B} = \mu \vec{H}$, $\vec{J} = \sigma \vec{E}$, and $\vec{J}_m = \sigma_m \vec{H}$. The ε and μ are the permittivity and permeability. The σ and σ_m are electric and magnetic conductivities.

In Cartesian coordinates, Eqs. (1) and (2) are written as

$$\begin{aligned}
&\frac{\partial H_z(x,y,z,t)}{\partial y} - \frac{\partial H_y(x,y,z,t)}{\partial z} \\
&= \varepsilon \frac{\partial E_x(x,y,z,t)}{\partial t} + \sigma E_x(x,y,z,t), \\
&\frac{\partial H_x(x,y,z,t)}{\partial z} - \frac{\partial H_z(x,y,z,t)}{\partial x} \\
&= \varepsilon \frac{\partial E_y(x,y,z,t)}{\partial t} + \sigma E_y(x,y,z,t), \\
&\frac{\partial H_y(x,y,z,t)}{\partial x} - \frac{\partial H_x(x,y,z,t)}{\partial y} \\
&= \varepsilon \frac{\partial E_z(x,y,z,t)}{\partial t} + \sigma E_z(x,y,z,t),
\end{aligned} \quad (3)$$

and

$$\begin{aligned}
&\frac{\partial E_z(x,y,z,t)}{\partial y} - \frac{\partial E_y(x,y,z,t)}{\partial z} \\
&= -\mu \frac{\partial H_x(x,y,z,t)}{\partial t} - \sigma_m H_x(x,y,z,t), \\
&\frac{\partial E_x(x,y,z,t)}{\partial z} - \frac{\partial E_z(x,y,z,t)}{\partial x} \\
&= -\mu \frac{\partial H_y(x,y,z,t)}{\partial t} - \sigma_m H_y(x,y,z,t), \\
&\frac{\partial E_y(x,y,z,t)}{\partial x} - \frac{\partial E_x(x,y,z,t)}{\partial y} \\
&= -\mu \frac{\partial H_z(x,y,z,t)}{\partial t} - \sigma_m H_z(x,y,z,t).
\end{aligned} \quad (4)$$

Equations (3) and (4) are solved by the finite-difference time-domain (FDTD) method. In this paper, we use the proprietary software LUMERICAL FDTD SOLUTIONS that implements the FDTD method to obtain the plasmonic field $\vec{E}$ [40–42]. As illustrated in Fig. 1, the bow-tie nanostructure is characterized by four geometrical parameters: height (h), angle (θ), thickness (t), and gap (d). The nanostructure is made of gold, whose wavelength-dependent complex dielectric constants are taken from Palik data [43]. We choose a 5.3-fs, 800-nm laser pulse with the intensity of 6.0×10^{11} W/cm^2 as the incident pulse. The incident pulse is linearly polarized along the x direction. The spatial range V_n in our simulation is $500\times400\times100$ nm with a spatial step of 1 nm. The total simulation time is 100 fs with a time step of 2.9 as. Based on our simulation, we find that in our case, the y component and z component of plasmonic field $E_y(x,y,z,t)$ and $E_z(x,y,z,t)$ are equal to 0. Therefore the x component of plasmonic field $E_x(x,y,z,t)$ is extracted for driving the HHG process.

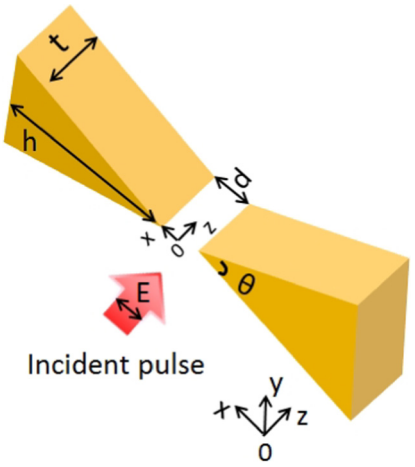

FIG. 1. Geometry of a single bow-tie nanostructure. The incident pulse linearly polarizes along the x direction.

B. Single-atom response

Second, we solve the time-dependent Schrödinger equation (TDSE) to model the single-atom response of the plasmon-driven HHG [39,44]. The TDSE in one spatial dimension is expressed as

$$\begin{aligned}
i\frac{\partial \psi(x,t)}{\partial t} &= H(t)\psi(x,t) \\
&= \left[-\frac{1}{2}\frac{\partial^2}{\partial x^2} + V_{\text{atom}}(x) + V(x,t)\right],
\end{aligned} \quad (5)$$

where $H(t)$ and $\psi(t)$ are the Hamiltonian and the electron wave function, respectively. The Coulomb potential $V_{\text{atom}}(x)$ is described by

$$V_{\text{atom}}(x) = -\frac{1}{\sqrt{x^2+\varepsilon}}, \quad (6)$$

where the soft core parameter ε is equal to 1.415 for the gas medium argon that is injected into the nanogap. The potential $V(x,t)$ represents the interaction of the atomic electron and laser field. It is given by

$$V(x,t) = E_x(x+x_0,y_0,z_0,t)x, \quad (7)$$

where $E_x(x+x_0,y_0,z_0,t)$ is the x component of plasmonic field. (x_0,y_0,z_0) represents the coordinate of any spatial point. For comparison, we also calculate the single-atom harmonic

spectrum in the spatially homogeneous field. In this case, the potential is given by $V(t) = E_x(x_0,y_0,z_0,t)x$.

Equation (5) is solved by the split-operator method [45]. In order to prevent spurious reflections and guarantee that the wave-packet components near the metallic surface can be absorbed, the time-dependent wave function at each time step times a smooth $\sin^{\frac{1}{8}}$ function. This function changes from 1 to 0 from the spatial point (x_0,y_0,z_0) to the edge of the metallic surface ($x_0 = \pm 10$ nm) [39].

Then, the generated harmonics can be calculated by the time-dependent dipole acceleration $a(t)$, which is given by

$$a(t) = \frac{d^2\langle x\rangle}{dt^2} = -\langle\psi(t)|[H(t),[H(t),x]]|\psi(t)\rangle. \quad (8)$$

The harmonic spectrum is then obtained by Fourier transforming the dipole acceleration $a(t)$:

$$a_q = \left|\frac{1}{\tau}\int_0^\tau a(t)\exp(-iq\omega t)\right|^2, \quad (9)$$

where q is the harmonic order.

C. The propagation of high harmonics

Finally, we solve the propagation equation for the harmonic field E_h in Cartesian coordinates [46,47], which is expressed as

$$\nabla^2 E_h(x,y,z,t) - \frac{1}{c^2}\frac{\partial^2 E_h(x,y,z,t)}{\partial t^2} = \frac{\omega_p^2(x,y,z,t)}{c^2}E_h(x,y,z,t) + \mu_0\frac{\partial^2 P(x,y,z,t)}{\partial t^2}, \quad (10)$$

where, $\nabla^2 = \nabla_\perp^2 + \partial^2/\partial z^2$, $\nabla_\perp^2 = \partial^2/\partial x^2 + \partial^2/\partial y^2$, and c is the speed of light. $\omega_p = e[4\pi n_e(t)/m_e]^{1/2}$ is the plasma frequency, m_e and e are the mass and charge of an electron. $n_e(t) = n_0[1-\exp(-\int_{-\infty}^t \gamma(t')dt')]$ is the free-electron density in the gas. $n_0(m^{-3})$ is the density of the gas medium, which is given by $3.5\times10^{22}\times p(\text{torr})$. p is the gas pressure, which is set to 10 torr in our calculation. $\gamma(t)$ is the ionization rate, which is calculated by the Ammosov-Delone-Krainov (ADK) theory [48]. By using a moving coordinate frame $z' = z$ and $t' = t - z/c$, Eq. (10) becomes

$$\nabla_\perp^2 E_h(x,y,z',t') - \frac{2}{c}\frac{\partial^2 E_h(x,y,z',t')}{\partial z'\partial t'} = \frac{\omega_p^2(x,y,z',t')}{c^2}E_h(x,y,z',t') + \mu_0\frac{\partial^2 P(x,y,z',t')}{\partial t'^2}, \quad (11)$$

the temporal derivative in Eq. (11) can be eliminated by Fourier transform, yielding the equation,

$$\nabla_\perp^2 \tilde{E}_h(x,y,z',\omega) - \frac{2i\omega}{c}\frac{\partial \tilde{E}_h(x,y,z',\omega)}{\partial z'} = \hat{F}\left[\frac{\omega_p^2(x,y,z',t')}{c^2}E_h(x,y,z',t')\right] - \omega^2\mu_0\tilde{P}(x,y,z',\omega), \quad (12)$$

$\tilde{E}_h(x,y,z',\omega) = \hat{F}[E_h(x,y,z',t')]$, $\tilde{P}(x,y,z',\omega) = \hat{F}[P(x,y,z',t')]$. $\hat{F}$ is the Fourier transform operator acting on the temporal coordinate. The polarization $\tilde{P}(x,y,z',\omega) = \tilde{P}_{nl}(x,y,z',\omega) + \chi^{(1)}\tilde{E}_h(x,y,z',\omega)$, where the nonlinear polarization $\tilde{P}_{nl}(x,y,z',\omega) = \hat{F}\{[n_0 - n_e(x,y,z',t')]D(x,y,z',t')\}$. The single-atom-induced dipole moment $D(x,y,z',t')$ can be obtained by the dipole acceleration $a(t)$. $a(t)$ is calculated at each grid point by using the corresponding spatially dependent plasmonic field E_x that is extracted from LUMERICAL FDTD SOLUTIONS. The linear susceptibility $\chi^{(1)}$ [49] can be obtained by the refractive index $n(\omega) = \sqrt{(1+\chi^{(1)}(\omega)/\varepsilon_0)}$, $n(\omega) = 1 - \delta_h(\omega) - i\beta_h(\omega) = 1 - \frac{1}{2\pi}n_0 r_0\lambda^2(f_1+f_2)$, and n_0 is again the gas density. r_0 is the classical electron radius, λ is the input pulse wavelength, and f_1 and f_2 are atomic scattering factors which can be obtained from Refs. [50,51]. $\delta_h(\omega)$ and $\beta_h(\omega)$ account for the dispersion and absorption of the gas medium on the harmonics, respectively.

Equation (12) is solved by using the Crank-Nicholson method. In our simulation of macroscopic HHG, we assume that the gas atoms are evenly distributed in the spatial range $20\times20\times30$ nm and the spatial range is split evenly with a spatial step of 1 nm. We first calculate 400 (20×20) single-atom dipole acceleration $a(t)$ via Eq. (5) and the ionization probability via the ADK theory on the initial plane ($z' = 0$ nm). In this calculation, the spatially dependent plasmonic fields E_x are extracted from LUMERICAL FDTD SOLUTIONS. Then, we insert the 400 single-atom dipole acceleration $a(t)$ and the ionization probability into Eq. (12) to obtain the high-order harmonics on the next plane ($z_1 = z' + \triangle z'$). Repeating this procedure, we obtain the final high harmonics at the exit face of the single bow-tie nanostructure ($z' = 30$ nm). Finally, by spatially integrating the final high harmonics at the exit face of the single bow-tie nanostructure, we can gain the macroscopic harmonic spectrum from gas-exposed single bow-tie nanostructure.

III. RESULTS AND DISCUSSIONS

In Fig. 2(a), we show the enhancement factor of field intensity as a function of the bow-tie height and angle. Here, the bow-tie thickness and gap are 30 nm and 20 nm, respectively. One can see that when the bow-tie height and angle are 180 nm and 80°, the field enhancement factor reaches maximum (∼50). Under this condition, we show the plasmonic field intensity distributions in the nanogap for three planes: $z = 15$ nm [Fig. 2(b)], $y = 0$ nm [Fig. 2(c)], and $x = 0$ nm [Fig. 2(d)]. The intensity distributions are plotted at the peak of the plasmonic field ($t = 17.88$ fs) [Fig. 2(e)]. The intensity distributions are symmetric with respect to $x = 0$ nm, $y = 0$ nm, and $z = 15$ nm.

In Fig. 3(a), we show the single-atom harmonic spectrum in spatially homogeneous field. Here, the electric field is extracted from the spatial point $x_0 = 4$ nm, $y_0 = 0$ nm, and $z_0 = 15$ nm. One can see that the harmonic cutoff is around 65^{th}. It is extended to 205^{th} in the spatially inhomogeneous field [Fig. 3(b)]. The cutoff extension is because the electrons gain much higher kinetic energy to contribute to the harmonics around the cutoff in the inhomogeneous field than that in the homogenous field. Moreover, the harmonic spectrum in Fig. 3(b) presents a typical plateau structure. The intensities of harmonics in the plateau and cutoff regions are comparable. Figure 3(c) shows the plasmon-driven macroscopic harmonic spectrum. One can see that the harmonic intensities drop

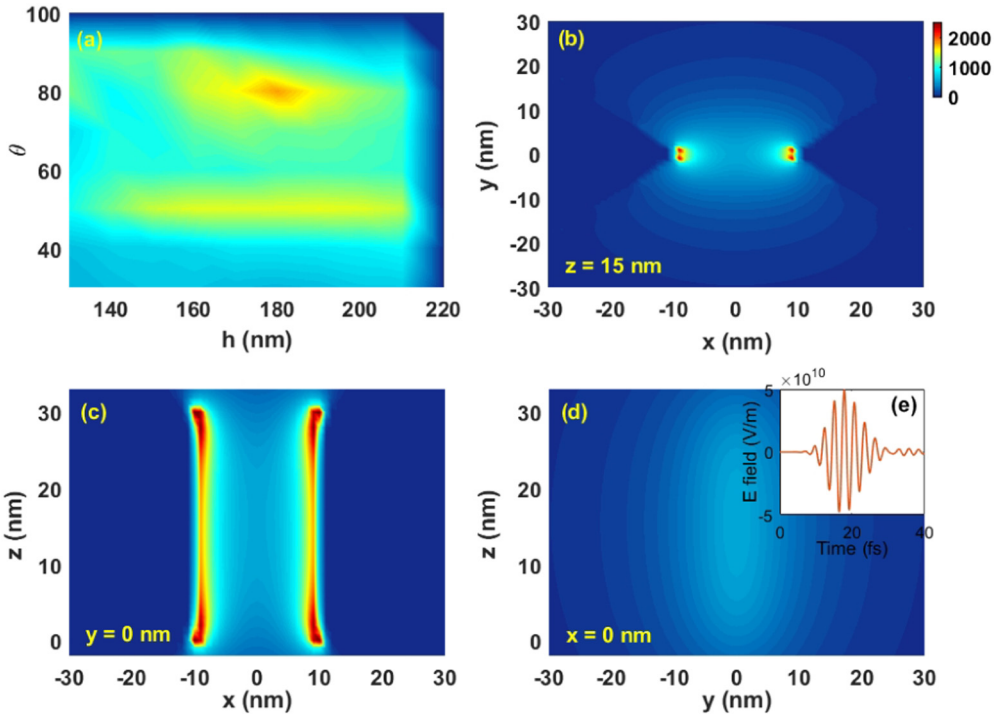

FIG. 2. (a) Enhancement factor of field intensity as a function of the bow-tie height and angle. (b)–(d) Spatial profile of plasmonic field in the plane of $z = 15$ nm, $y = 0$ nm, and $x = 0$ nm at $t = 17.88$ fs. (e) $E_x(t)$ at the point (0, 0, 15). Here, the geometrical parameters are $h = 180$ nm, $\theta = 80°$, $t = 30$ nm, and $d = 20$ nm.

dramatically as the harmonic order increases. The intensities of harmonics with high photon energy ($>100^{\text{th}}$) are nearly 10 orders of magnitude smaller than that with low photon energy

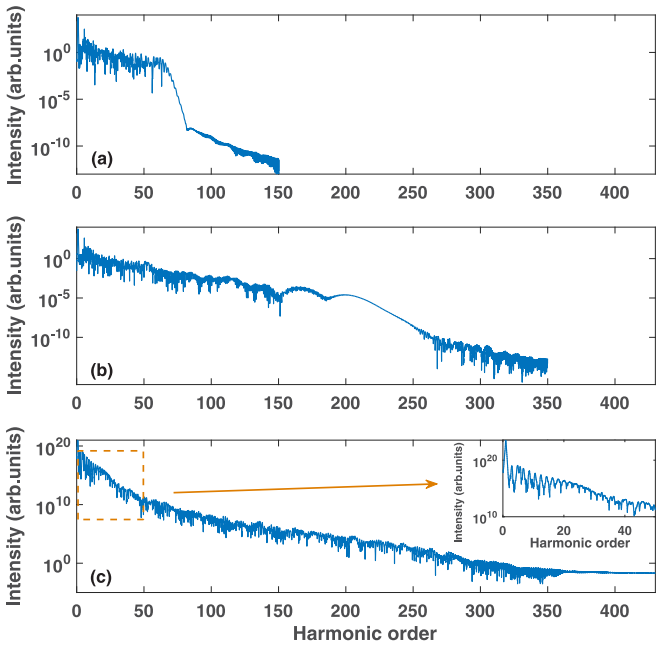

FIG. 3. (a) Single-atom harmonic spectrum in the spatially homogeneous field. (b) Single-atom harmonic spectrum in the spatial inhomogeneity field. (c) Plasmon-driven macroscopic harmonic spectrum. In Figs. 3(a) and 3(b), the spatial point is $x_0 = 4$ nm, $y_0 = 0$ nm, and $z_0 = 15$ nm.

($<30^{\text{th}}$). It is the reason why the harmonic cutoff observed in the experiment is much smaller than that calculated on the single-atom level.

To clarify the dramatic decline of high-energy harmonics in Fig. 3(c), we next calculate the plasmon-driven single-atom harmonic spectra at different spatial points in Fig. 4. In Fig. 4(a), we show the results along the positive-x direction. Here, y_0 and z_0 are equal to 0 nm and 15 nm. From Fig. 2(b), one can see that the field intensity gradually increases from $x_0 = 0$ nm to $x_0 = 4$ nm. Therefore, the harmonic cutoff at $x_0 = 4$ nm is extended compared with that at $x_0 = 0$ nm [Fig. 4(a)]. As the x_0 increases to 8 nm, the field intensity further increases [Fig. 2(b)], while the harmonic cutoff is shortened [Fig. 4(a)]. This is because the high-energy electrons ionized from the point $x_0 = 8$ nm are strongly absorbed by metallic surfaces. Figures 4(b) and 4(c) present the single-atom harmonic spectra at different spatial points along the positive-y ($x_0 = 0$ nm, $z_0 = 15$ nm) and z ($x_0 = 0$ nm, $y_0 = 0$ nm) directions. As shown in Fig. 2(d), the plasmonic field intensity gradually decreases along the positive-y direction. Therefore, the harmonic cutoff is gradually reduced as y_0 increases [Fig. 4(b)] Besides, the plasmonic field intensity presents the inverted U-shaped distribution along the z direction. As a consequence, the harmonic cutoffs at $z_0 = 0$ and 30 nm are the same, which are smaller than that at $z_0 = 15$ nm [Fig. 4(c)]. In short, the cutoff position of the plasmon-driven single-atom harmonic spectrum depends sensitively on the spatial position. Furthermore, we note that only a few spatial points in the vicinity of nanostructure contribute to the harmonic emission with high energy. Therefore, the intensities of macroscopic harmonics fall dramatically in the high-energy region as shown in Fig. 3(c).

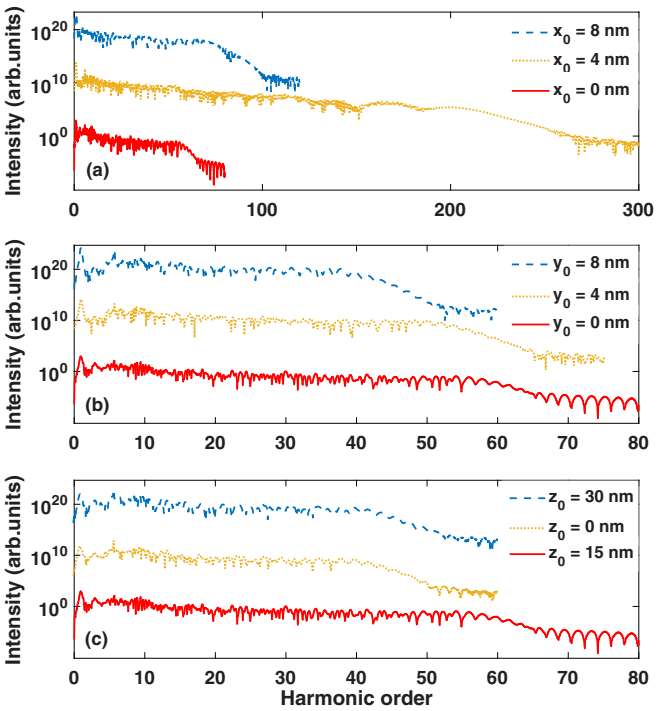

FIG. 4. (a) Plasmon-driven single-atom harmonic spectra at the spatial points (0, 0, 15), (4, 0, 15), and (8, 0, 15). (b) and (c) Same as (a), but at the spatial points (0, 0, 15), (0, 4, 15) (0, 8, 15) and (0, 0, 0), (0, 0, 15), (0, 0, 30). For easier comparison, the harmonic intensity is multiplied by a factor $10^{(10n-10)}$ with n changes from 1 to 3 from bottom to top in Figs. 4(a)–4(c).

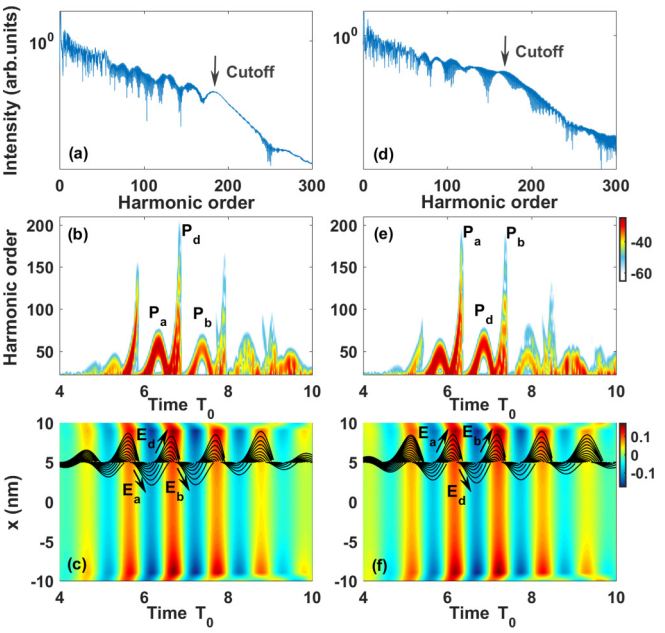

FIG. 5. (a)–(c) Plasmon-driven single-atom harmonic spectrum, time-frequency image and classical electron trajectories (black lines) of HHG at the spatial point (5, 0, 15) with the CEP of 0. (d)–(f). Same as (a)–(c), but with the CEP of π. The background color in Figs. 5(c) and 5(f) represents the distribution of the the plasmonic field amplitude E_x as a function of x and t.

Except for the cutoff extension, the previous work about plasmon-driven single-atom HHG also present that the harmonic cutoff with the CEP of 0 is larger than that of π [37,38]. While in the following, we will demonstrate that the cutoff difference with the CEP of 0 and π depends sensitively on the spatial position when considering the spatial distribution of plasmonic field in the nanogap.

In Fig. 5(a), we show the plasmon-driven harmonic spectrum at the point $x_0 = 5$ nm with the CEP of 0. Here, $y_0 = 0$ nm and $z_0 = 15$ nm. The harmonic cutoff is around 185^{th}, which is a little larger than that (169^{th}) with the CEP of π [Fig. 5(d)]. It is consistent with that in the previous reports [37,38]. This phenomenon can be well understood by analyzing the time-frequency properties and classical electron trajectories of HHG. As shown in Fig. 5(b), with the CEP of 0, the harmonic cutoff is determined by the highest photon-energy peak P_d. Figure 5(c) shows the corresponding electron trajectories. The electron trajectories that contribute to the peaks P_a, P_b, and P_d are marked as E_a, E_b, and E_d, respectively. One can see that the electron of E_d is ionized around $6T_0$ (T_0 is the optical cycle of the laser pulse) and then accelerated toward the positive-x direction where E_x gradually increases. In contrast, the electrons of E_a and E_b are accelerated toward the negative-x direction where E_x gradually decreases. Therefore, the peaks P_a and P_b are suppressed while the peak P_d is extended as shown in Fig. 5(b). When the laser field is reversed (CEP $= \pi$), the harmonic cutoff is determined by the peaks P_a and P_b [Fig. 5(e)]. From Fig. 5(f), one can see that the electrons of E_a and E_b are accelerated toward the positive-x direction. The electron of E_d is accelerated toward the negative-x direction. Therefore, the peak P_d is suppressed while the peaks P_a and P_b are extended as shown in Fig. 5(e). Since the electron of E_d is accelerated around the peak of laser field ($t = 6T_0 = 17.88$ fs), the harmonic cutoff with the CEP of 0 in Fig. 5(a) is larger than that with the CEP of π in Fig. 5(d).

In Fig. 6, we investigate the CEP effect on the harmonic emissions at the spatial point $x_0 = -5$ nm, $y_0 = 0$ nm, and $z_0 = 15$ nm. In the vicinity of this point [Figs. 6(c) and 6(f)], the electron that moves toward the positive- or negative-x direction feels the decreasing or increasing E_x. It is opposite to that at $x_0 = 5$ nm [Figs. 5(c) and 5(f)]. Therefore, with the CEP of 0, the peak P_d is suppressed and the peaks P_a and P_b are extended [Fig. 6(b)]. With the CEP of π, the peak P_d is extended and the peaks P_a and P_b are suppressed [Fig. 6(e)]. As a consequence, the harmonic cutoff with the CEP of 0 is smaller than that of π [Figs. 6(a) and 6(d)]. Moreover, since E_x is symmetric with respect to the $x = 0$ nm, the harmonic spectrum of Fig. 6(a) is the same as that with the CEP of π at $x_0 = 5$ nm in Fig. 5(d). The harmonic spectrum of Fig. 6(d) is the same as that with the CEP of 0 at $x_0 = 5$ nm in Fig. 5(a).

Figure 7 shows the CEP-dependent harmonic emissions at the spatial point $x_0 = 0$ nm, $y_0 = 0$ nm, and $z_0 = 15$ nm. Since E_x is symmetric with respect to $x = 0$ nm, the electron of E_d is accelerated along the positive- (negative)-x direction (CEP $= 0/\pi$) and feels the same field distribution [Figs. 7(c) and 7(f)]. Therefore, the harmonic spectra with the CEP of 0 and π are the same as shown in Figs. 7(a) and 7(d). To sum up, the cutoff difference induced by a π shift in the CEP of the laser pulse depends sensitively on the spatial position. For two symmetric

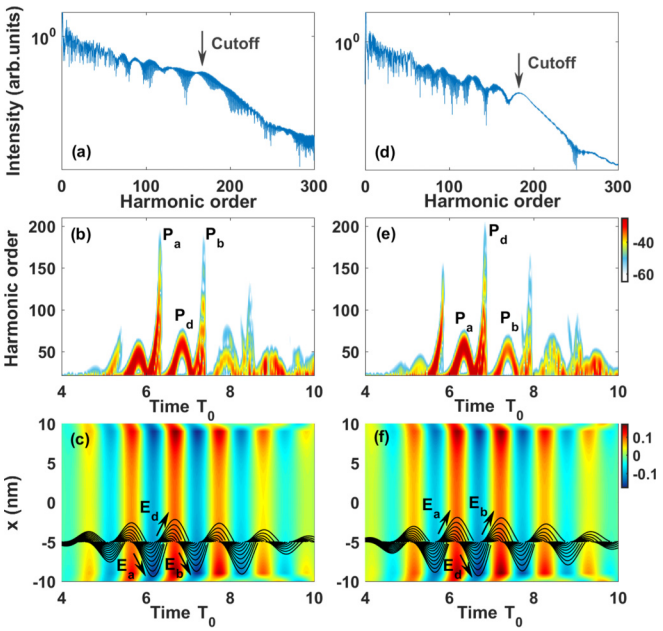

FIG. 6. Same as Fig. 5, but at the spatial point (−5, 0, 15).

spatial points along the x direction, the CEP dependence is opposite. Therefore, when spatially integrating the final harmonics at the exit of the bow-tie nanostructure (Fig. 8), the macroscopic harmonic spectra obtained by a π shift in the CEP of the laser pulses keep the same, which is different from the previous reports on the single-atom level [37,38].

Finally, it must be noted that in our work, we only calculate the macroscopic harmonic spectrum from gas-exposed single bow-tie nanostructure rather than an array of bow-tie nanostructures as in Kim's experiment [18]. For an array of bow-tie nanostructures placed perpendicular to the propagation axis, each single bow-tie nanostructure acts as a pointlike source.

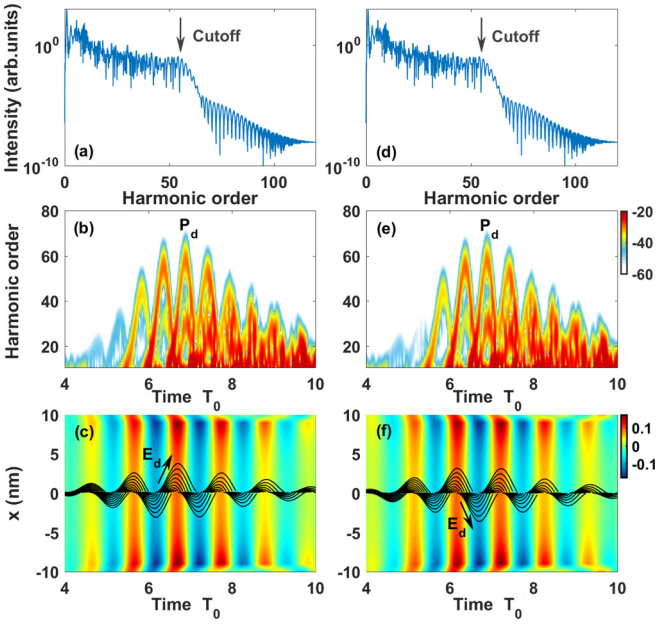

FIG. 7. Same as Fig. 5, but at the spatial point (0, 0, 15).

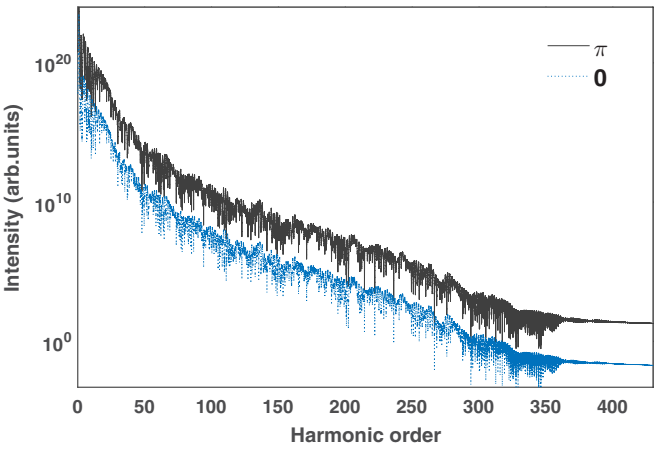

FIG. 8. Macroscopic harmonic spectra with the CEP of 0 and π. The harmonic intensity with the CEP of π is multiplied by a factor 10^3 for easier comparison.

When the size of the array is much smaller than the beam waist of Guassian laser field, the harmonic radiations coming from each bow-tie nanostructure will be a coherent superposition. However, when the size of the array is comparable to the beam waist of Guassian laser field, the laser intensity quickly changes along the radial direction (x or y direction) of the array. Then, the transversal phase mismatching [52] may play a role in the propagation and it will influence the intensities of plasmon-driven macroscopic harmonics in the plateau structure.

IV. CONCLUSION

We report a numerical method to calculate the plasmon-driven macroscopic harmonic spectrum. This method includes the propagation of plasmonic and harmonic fields in the macroscopic medium as well as the single-atom response of HHG. Based on the simulation, we find that only a few spatial points in the vicinity of the nanostructure can contribute to the high-energy harmonics. Therefore, the intensities of plasmon-driven macroscopic harmonics with high energy drop dramatically. It well clarifies the discrepancy in the cutoff between the single-atom harmonic spectrum and the experiments [18]. Moreover, we show that the cutoff difference induced by a π shift in the CEP of the laser pulse depends sensitively on the spatial position. When the spatial point is located in $x_0 = 0$ nm, the harmonic cutoffs with the CEP of 0 and π are the same. When the spatial point is located in the positive (negative) x axis, the harmonic cutoff with the CEP of 0 is larger (smaller) than that with the CEP of π. Due to the spatial symmetry and time inversion symmetry of plasmonic field in the nanogap, the macroscopic harmonic spectra obtained by a π shift in the CEP of the laser pulses keep the same. Our method provides a tool for better investigating the HHG process in the nanostructure.

ACKNOWLEDGMENTS

This work was supported by National Natural Science Foundation of China under Grants No. 61275126, No.

11404123, No. 11422435, and No. 11234004. Numerical simulations presented in this paper were carried out using the High Performance Computing experimental test bed in SCTS/CGCL.

[1] E. Goulielmakis, M. Schultze, M. Hofstetter, V. S. Yakovlev, J. Gagnon, M. Uiberacker, A. L. Aquila, E. M. Gullikson, D. T. Attwood, R. Kienberger, F. Krausz, and U. Kleineberg, Science **320**, 1614 (2008).

[2] P. Lan, P. Lu, W. Cao, Y. Li, and X. Wang, Phys. Rev. A **76**, 051801 (2007); W. Hong, P. Wei, Q. Zhang, S. Wang, and P. Lu, Opt. Express **18**, 11308 (2010).

[3] M. Chen, C. Mancuso, C. Hernández-García, F. Dollar, B. Galloway, D. Popmintchev, P. Huang, B. Walker, L. Plaja, A. Jaroń-Becker, A. Becker, M. Murnane, H. Kapteyn, and T. Popmintchev, Proc. Natl. Acad. Sci. USA **111**, E2361 (2014).

[4] D. Popmintchev, C. Herández-García, F. Dollar, C. Mancuso, J. A. Pérez-Hernández, M.-C. Chen, A. Hankla, X. Gao, B. Shim, A. L. Gaeta, M. Tarazkar, D. A. Romanov, R. J. Levis, J. A. Gaffney, M. Foord, S. B. Libby, A. Jaron-Becker, A. Becker, L. Plaja, M. M. Murnane, H. C. Kapteyn, and T. Popmintchev, Science **350**, 1225 (2015).

[5] S. A. Rezvani, Z. Hong, X. Pang, S. Wu, Q. Zhang, and P. Lu, Opt. Lett. **42**, 3367 (2017); Z. Hong, Q. Zhang, S. A. Rezvani, P. Lan, and P. Lu, Opt. Laser Technol. **98**, 169 (2018).

[6] K. Zhao, Q. Zhang, M. Chini, Y. Wu, X. Wang, and Z. Chang, Opt. Lett. **37**, 3891 (2012).

[7] E. Goulielmakis, Z. Loh, A. Wirth, R. Santra, N. Rohringer, V. S. Yakovlev, S. Zherebtsov, T. Pfeifer, A. M. Azzeer, M. F. Kling, S. R. Leone, and F. Krausz, Nature (London) **466**, 739 (2010).

[8] L. Li, X. Zhu, P. Lan, L. He, and P. Lu, arXiv:1702.04084; L. Li, Z. Wang, F. Li, and H. Long, Opt Quantum Electron **49**, 73 (2017).

[9] S. Baker, J. S. Robinson, C. A. Haworth, H. Teng, R. A. Smith, C. C. Chirilă, M. Lein, J. W. G. Tisch, and J. P. Marangos, Science **312**, 424 (2006).

[10] P. Lan, M. Ruhmann, L. He, C. Zhai, F. Wang, X. Zhu, Q. Zhang, Y. Zhou, M. Li, M. Lein, and P. Lu, Phys. Rev. Lett. **119**, 033201 (2017); X. Liu, P. Li, X. Zhu, P. Lan, Q. Zhang, and P. Lu, Phys. Rev. A **95**, 033421 (2017).

[11] B. K. McFarland, J. P. Farrell, P. H. Bucksbaum, and M. Gühr, Science **322**, 1232 (2008).

[12] C. Zhai, X. Zhu, P. Lan, F. Wang, L. He, W. Shi, Y. Li, M. Li, Q. Zhang, and P. Lu, Phys. Rev. A **95**, 033420 (2017); M. Qin and X. Zhu, Opt. Laser Technol. **87**, 79 (2017).

[13] K. Lin, P. Lu, J. Ma, X. Gong, Q. Song, Q. Ji, W. Zhang, H. Zeng, J. Wu, G. Karras, G. Siour, J. M. Hartmann, O. Faucher, E. Gershnabel, Y. Prior, and I. S. Averbukh, Phys. Rev. X **6**, 041056 (2016).

[14] O. Korech, U. Steinitz, R. J. Gordon, I. S. Averbukh, and Y. Prior, Nat. Photon. **7**, 711 (2013).

[15] A. L. Cavalieri, N. Müller, Th. Uphues, V. S. Yakovlev, A. Baltuška, B. Horvath, B. Schmidt, L. Blümel, R. Holzwarth, S. Hendel, M. Drescher, U. Kleineberg, P. M. Echenique, R. Kienberger, F. Krausz, and U. Heinzmann, Nature (London) **449**, 1029 (2007).

[16] T. Y. Du, Z. Guan, X. X. Zhou, and X. B. Bian, Phys. Rev. A **94**, 023419 (2016).

[17] X. Liu, X. Zhu, P. Lan, X. Zhang, D. Wang, Q. Zhang, and P. Lu, Phys. Rev. A **95**, 063419 (2017).

[18] S. Kim, J. Jin, Y.-J. Kim, I.-Y. Park, Y. Kim, and S.-W. Kim, Nature (London) **453**, 757 (2008).

[19] G. Vampa, B. G. Ghamsari, S. Siadat Mousavi, T. J. Hammond, A. Olivier, E. Lisicka-Skrek, A. Yu Naumov, D. M. Villeneuve, A. Staudte, P. Berini, and P. B. Corkum, Nat. Phys. **13**, 659 (2017).

[20] S. Han, H. Kim, Y. W. Kim, Y.-J. Kim, S. Kim, I.-Y. Park, and S.-W. Kim, Nat. Commun. **7**, 13105 (2016).

[21] N. Pfullmann *et al.*, Ann. Phys. **526**, 119 (2014).

[22] I.-Y. Park, S. Kim, J. Choi, D.-H. Lee, Y.-J. Kim, M. F. Kling, M. I. Stockman, and S.-W. Kim, Nat. Photon. **5**, 677 (2011).

[23] M. Krebs, S. Hädrich, S. Demmler, J. Rothhardt, A. Zaïr, L. Chipperfield, J. Limpert, and A. Tünnermann, Nat. Photon. **7**, 555 (2013).

[24] M. Sivis, M. Duwe, B. Abel, and C. Ropers, Nat. Phys. **9**, 304 (2013).

[25] M. Sivis, M. Duwe, B. Abel, and C. Ropers, Nature (London) **485**, E1 (2012).

[26] S. Kim, J. Jin, Y.-J. Kim, I.-Y. Park, Y. Kim, and S.-W. Kim, Nature (London) **485**, E2 (2012).

[27] M. F. Ciappina, J. A. Pérez-Hernández, A. S. Landsman, W. A. Okell, S. Zherebtsov, B. Forg, J. Schötz, L. Seiffert, T. Fennel, T. Shaaran, T. Zimmermann, A. Chacón, R. Guichard, A. Zaïr, J. W. G. Tisch, J. P. Marangos, T. Witting, A. Braun, S. A. Maier, L. Roso, M. Krüger, P. Hommelhoff, M. F. Kling, F. Krausz, and M. Lewenstein, Rep. Prog. Phys. **80**, 054401 (2017).

[28] M. Lupetti, M. F. Kling, and A. Scrinzi, Phys. Rev. Lett. **110**, 223903 (2013).

[29] S. Choi, M. F. Ciappina, J. A. Pérez-Hernández, A. S. Landsman, Y.-J. Kim, S. C. Kim, and D. Kim, Phys. Rev. A **93**, 021405(R) (2016).

[30] I.-Y. Park, S. Kim, J. Choi, D.-H. Lee, and S.-W. Kim, Proc. SPIE **8096**, 80960S (2011).

[31] J. A. Pérez-Hernández, M. F. Ciappina, M. Lewenstein, L. Roso, and A. Zaïr, Phys. Rev. Lett. **110**, 053001 (2013).

[32] T. Shaaran, M. F. Ciappina, and M. Lewenstein, Phys. Rev. A **86**, 023408 (2012).

[33] A. Husakou, S.-J. Im, and J. Herrmann, Phys. Rev. A **83**, 043839 (2011).

[34] M. F. Ciappina, J. Biegert, R. Quidant, and M. Lewenstein, Phys. Rev. A **85**, 033828 (2012).

[35] J. Luo, Y. Li, Z. Wang, Q. Zhang, and P. Lu, J. Phys. B **46**, 145602 (2013); J. Luo, Y. Li, Z. Wang, L. He, Q. Zhang, P. Lan, and P. Lu, Phys. Rev. A **89**, 023405 (2014).

[36] M. F. Ciappina, S. S. Aćimović, T. Shaaran, J. Biegert, R. Quidant, and M. Lewenstein, Opt. Express **20**, 26261 (2012).

[37] J. Choi, S. Kim, I.-Y. Park, D.-H. Lee, S. Han, and S.-W. Kim, New J. Phys. **14**, 103038 (2012).

[38] I. Yavuz, E. A. Bleda, Z. Altun, and T. Topcu, Phys. Rev. A **85**, 013416 (2012).

[39] I. Yavuz, Phys. Rev. A **87**, 053815 (2013).
[40] D. P. Fromm, A. Sundaramurthy, P. James Schuck, G. Kino, and W. E. Moerner, Nano Lett. **4**, 957 (2004); Z. Wang, B. Wang, H. Long, K. Wang, and P. Lu, J. Lightw. Technol. **35**, 2960 (2017).
[41] E. Skopalová, D. Y. Lei, T. Witting, C. Arrell, F. Frank, Y. Sonnefraud, S. A. Maier, J. W. G. Tisch, and J. P. Marangos, New J. Phys. **13**, 083003 (2011).
[42] A. F. Oskooi, D. Roundy, M. Ibanescu, P. Bermel, J. D. Joannopoulos, and S. G. Johnson, Comput. Phys. Commun. **181**, 687 (2010).
[43] E. D. Palik, *Handbook of Optical Constants of Solids* (Academic Press, New York, 1997).
[44] L. He, Z. Wang, Y. Li, Q. Zhang, P. Lan, and P. Lu, Phys. Rev. A **88**, 053404 (2013); Z. Wang, P. Lan, J. Luo, L. He, Q. Zhang, and P. Lu, *ibid.* **88**, 063838 (2013).
[45] M. D. Feit, J. A. Fleck, and A. J. R. Steiger, J. Comput. Phys. **47**, 412 (1982).
[46] P. Lan, P. Lu, Q. Li, F. Li, W. Hong, and Q. Zhang, Phys. Rev. A **79**, 043413 (2009); F. Wang, L. He, C. Zhai, W. Shi, Q. Zhang, P. Lan, and P. Lu, *ibid.* **92**, 063839 (2015).
[47] C. Jin, A. T. Le, and C. D. Lin, Phys. Rev. A **83**, 023411 (2011).
[48] M. V. Ammosov, N. B. Delone, and V. P. Krainov, Sov. Phys. JETP **64**, 1191 (1986).
[49] R. W. Boyd, *Nonlinear Optics*, 2nd ed. (Academic Press, San Diego, 2003).
[50] C. T. Chantler, K. Olsen, R. A. Dragoset, J. Chang, A. R. Kishore, S. A. Kotochigova, and D. S. Zucker, *X-ray Form Factor*, Attenuation and Scattering Tables (Version 2.1) (National Institute of Standards and Technology, Gaithersburg, MD, 2005); http://physics.nist.gov/ffast
[51] B. L. Henke, E. M. Gullikson, and J. C. Davis, At. Data Nucl. Data Tables **54**, 181 (1993).
[52] C. Hernández-García, I. J. Sola, and L. Plaja, Phys. Rev. A **88**, 043848 (2013).